

Homology modeling and molecular dynamics simulation of *N*-myristoyltransferase from protozoan parasites: active site characterization and insights into rational inhibitor design

Chunquan Sheng · Haitao Ji · Zhenyuan Miao · Xiaoyin Che ·
Jianzhong Yao · Wenya Wang · Guoqiang Dong ·
Wei Guo · Jianguo Lü · Wannian Zhang

Received: 18 December 2008 / Accepted: 26 March 2009 / Published online: 16 April 2009
© Springer Science+Business Media B.V. 2009

Abstract Myristoyl-CoA:protein *N*-myristoyltransferase (NMT) is a cytosolic monomeric enzyme that catalyzes the transfer of the myristoyl group from myristoyl-CoA to the N-terminal glycine of a number of eukaryotic cellular and viral proteins. Recent experimental data suggest NMT from parasites could be a promising new target for the design of novel antiparasitic agents with new mode of action. However, the active site topology and inhibitor specificity of these enzymes remain unclear. In this study, three-dimensional models of NMT from *Plasmodium falciparum* (PfNMT), *Leishmania major* (LmNMT) and *Trypanosoma brucei* (TbNMT) were constructed on the basis of the crystal structures of fungal NMTs using homology modeling method. The models were further refined by energy minimization and molecular dynamics simulations. The active sites of PfNMT, LmNMT and TbNMT were characterized by multiple copy simultaneous search (MCSS). MCSS functional maps reveal that PfNMT, LmNMT and

TbNMT share a similar active site topology, which is defined by two hydrophobic pockets, a hydrogen-bonding (HB) pocket, a negatively-charged HB pocket and a positively-charged HB pocket. Flexible docking approaches were then employed to dock known inhibitors into the active site of PfNMT. The binding mode, structure–activity relationships and selectivity of inhibitors were investigated in detail. From the results of molecular modeling, the active site architecture and certain key residues responsible for inhibitor binding were identified, which provided insights for the design of novel inhibitors of parasitic NMTs.

Keywords Parasitic *N*-myristoyltransferase · Three-dimensional structures · Multiple copy simultaneous search · Active sites · Flexible molecular docking · Ligand selectivity

C. Sheng · Z. Miao · X. Che · J. Yao · W. Wang · G. Dong ·
W. Guo · J. Lü · W. Zhang (✉)
School of Pharmacy, Military Key Laboratory of Medicinal
Chemistry, Second Military Medical University, 325 Guohe
Road, 200433 Shanghai, People's Republic of China
e-mail: zhangwnk@hotmail.com

H. Ji
Department of Chemistry, Northwestern University, Evanston,
IL 60208-3113, USA

H. Ji
Department of Biochemistry, Molecular Biology, and Cell
Biology, Northwestern University, Evanston, IL 60208-3113,
USA

H. Ji
Center for Drug Discovery and Chemical Biology, Northwestern
University, Evanston, IL 60208-3113, USA

Introduction

Myristoyl-CoA:protein *N*-myristoyltransferase (NMT) is a cytosolic monomeric enzyme that catalyzes the transfer of the myristoyl group from myristoyl-CoA to the N-terminal glycine of a number of eukaryotic cellular and viral proteins [1, 2]. NMT follows an ordered bi–bi catalytic reaction mechanism [3, 4]. The apo-enzyme binds myristoyl-CoA to form a NMT myristoyl-CoA binary complex that is competent to acquire peptide substrates. A peptide substrate then binds to generate a myristoyl-CoA-NMT-peptide ternary complex. After the catalytic transfer of myristate from CoA to peptide substrate, CoA is released followed by myristoylpeptide. This co-translational modification relates to diverse biological processes including

signal transduction cascades and apoptosis [5–7]. Moreover, myristoylation of the proteins can result in increased lipophilicity, facilitating their association with cellular/subcellular membranes and mediating protein–protein interactions [8].

N-myristoyltransferase has been identified and characterized from a broad range of eukaryotic organisms including human [9, 10], animals [11], fungi [12–14] and protozoa [15, 16]. The many cellular functions of NMT have led to numerous investigations of this protein as a therapeutic target for the development of anticancer [17], antiviral [18], and antifungal [19] agents. Among them, most published work has been focused on NMT as an antifungal target. The X-ray crystal structures of NMT from *Candida albicans* (CaNMT) and *Saccharomyces cerevisiae* (ScNMT) have been determined in the apo form and in the binary or ternary complexes [20–24]. The availability of these crystal structures has provided important insights into the catalytic mechanism of NMT including conformational changes associated with substrate binding, key residues involved in stabilization of intermediates along the reaction pathway, the role of the oxyanion hole in the enzyme. Furthermore, the crystal structures of CaNMT have also accelerated the discovery of selective fungal NMT inhibitors as potential antifungal agents. The benzofuran [25–28] and benzothiazole [29, 30] inhibitors have shown micromolar (μM) to nanomolar (nM) inhibitory activity with excellent in vitro and in vivo antifungal activity.

Parasitic diseases are a major global health problem, which affect hundreds of millions of people worldwide [31]. Many of the drugs used today to treat diseases such as malaria, leishmaniasis, and African sleeping sickness were introduced decades ago and have many drawbacks, such as limited efficacy, ineffectivity against resistant organisms, and serious toxicity. The development of an antiparasitic drug with novel mode of action is a promising approach to decrease the morbidity and mortality caused by parasites. Investigations of NMT as an antiparasitic target are just emerging [32]. Comparative biochemical studies of NMT from *Plasmodium falciparum* (PfNMT) with human NMT (HsNMT) highlighted the potential of the enzyme for the development of selective antiparasitic compounds [15]. The biological experiments have shown NMT is an essential enzyme for viability in both *Leishmania major* and *Trypanosoma brucei*, respectively [16]. Up to now, only a few inhibitors of protozoan parasite NMTs have been reported [33, 34], which were previously discovered as fungal NMT inhibitors. In order to accelerate the discovery of novel inhibitors, the structural information of protozoan parasite NMTs is of great importance. However, the crystal structure of NMT from protozoan parasites has not been determined. Therefore, homology modeling of

parasitic NMT structures represents an alternative approach to rationalize the structure-based inhibitor design.

In the present investigation, we constructed three-dimensional (3D) structures of NMT from *Plasmodium falciparum* (PfNMT), *Leishmania major* (LmNMT) and *Trypanosoma brucei* (TbNMT), which are causative vectors of malaria, cutaneous leishmaniasis, and African sleeping sickness, respectively. The models were further refined by energy minimization and molecular dynamics simulations. The active sites of the modeled structures were characterized by multiple copy simultaneous search (MCSS). The binding mode and selectivity of PfNMT inhibitors were explored by flexible molecular docking.

Materials and methods

General

The crystallographic coordinates of CaNMT (3.2 Å resolution, $R_{\text{cryst}} = 0.288$) and ScNMT (3.0 Å resolution, $R_{\text{cryst}} = 0.263$) were obtained from the Protein Data Bank (PDB, entry code 1IYL and 2P6G) and used as templates. The primary sequences of PfNMT, LmNMT and HsNMT were obtained from the SwissProt database (accession number Q9U419, Q9GPZ4, and Q9UE09) and the TbNMT sequence was from Genome Survey Sequences (GSS) Database (accession number AL490833). All calculations were performed with commercially available InsightII 2000 software package on an Origin 300 Server.

Homology modeling

The sequences of PfNMT, LmNMT and TbNMT were aligned to CaNMT, ScNMT and HsNMT using the Align 123 module of InsightII. The Blosom-62 matrix was used with a gap penalty of 10 and a gap extension penalty of 1. Modeler module of InsightII 2000 was used to build the 3D models of PfNMT, LmNMT and TbNMT. Five cycles of modeler calculations were performed. During every modeler calculation cycle, five models were built with 10 loops generated to every model. During the model building, the optimize_level was set to medium and hydrogen atoms were not considered. The best models of PfNMT, LmNMT and TbNMT were then selected on the basis of the analysis result of internal scoring function of Modeller, Profile-3D program, and Procheck procedure [35].

The chosen models were then subjected to energy minimization. Hydrogen atoms were added to the models at pH 7 using the builder module of InsightII. The following parameters were used: Discover 95.0 Program of InsightII, CVFF force field, and steepest decent minimization, until an energy gradient tolerance of 1 kcal/mol Å was satisfied.

Energy minimization was started with the newly added hydrogen atoms, the loop side chains, the loop main chains, all the core side chains, and finally the core main chains. A conjugate gradient energy minimization of the full proteins was then performed until the rms gradient energy was lower than 0.001 kcal/mol Å.

MD simulation

Proteins were refined again using the CHARMM force field as implemented in InsightII. The atom types were assigned using the CHARMM force field and the distance-dependent dielectric constant four was employed for approximate solvent effects. The calculation included 100 steps of steepest descent (SD) minimization followed by 100 steps of conjugated gradient (CG) minimization. Unconstrained molecular dynamics simulation (The Verlet leapfrog integration method with temperature coupling) was then performed for 1.0 ns with 1.0 ps time intervals at 300 K after global minimization with the non-bonded cut-off set to 14 Å.

Model validation

The quality of the MD-refined output structures was assessed by a series of tests for its internal consistency and reliability. The ProStat module of InsightII was used to analyze the properties of bonds, angles, and torsions. The results revealed that the bond lengths and bond angles of the three models are not significantly different from the average values calculated from known proteins. The stereochemical quality of the modeled protein structures was examined by the PROCHECK program [35] through a Ramachandran plot. The Profile-3D program [36] in InsightII was used to evaluate the fitness of the models sequence in their current 3D environment. The root mean square deviation (RMSD) between the main chain atoms of the models and templates was calculated for the reliability of the models. Finally, the best quality model of PfNMT, LmNMT and TbNMT was chosen for further calculations and molecular modeling studies.

Binding site analysis

Binding site analysis module within InsightII was used to identify the active sites of PfNMT, LmNMT and TbNMT. The grid size was set to 1 Å × 1 Å × 1 Å. All of the solvent accessible surfaces in the proteins were filled with grid points and only those having at least 125 grid points were accepted as possible active sites. After comparing with the position of the active sites in the crystal structures of CaNMT and ScNMT, the binding sites of PfNMT, LmNMT and TbNMT were determined.

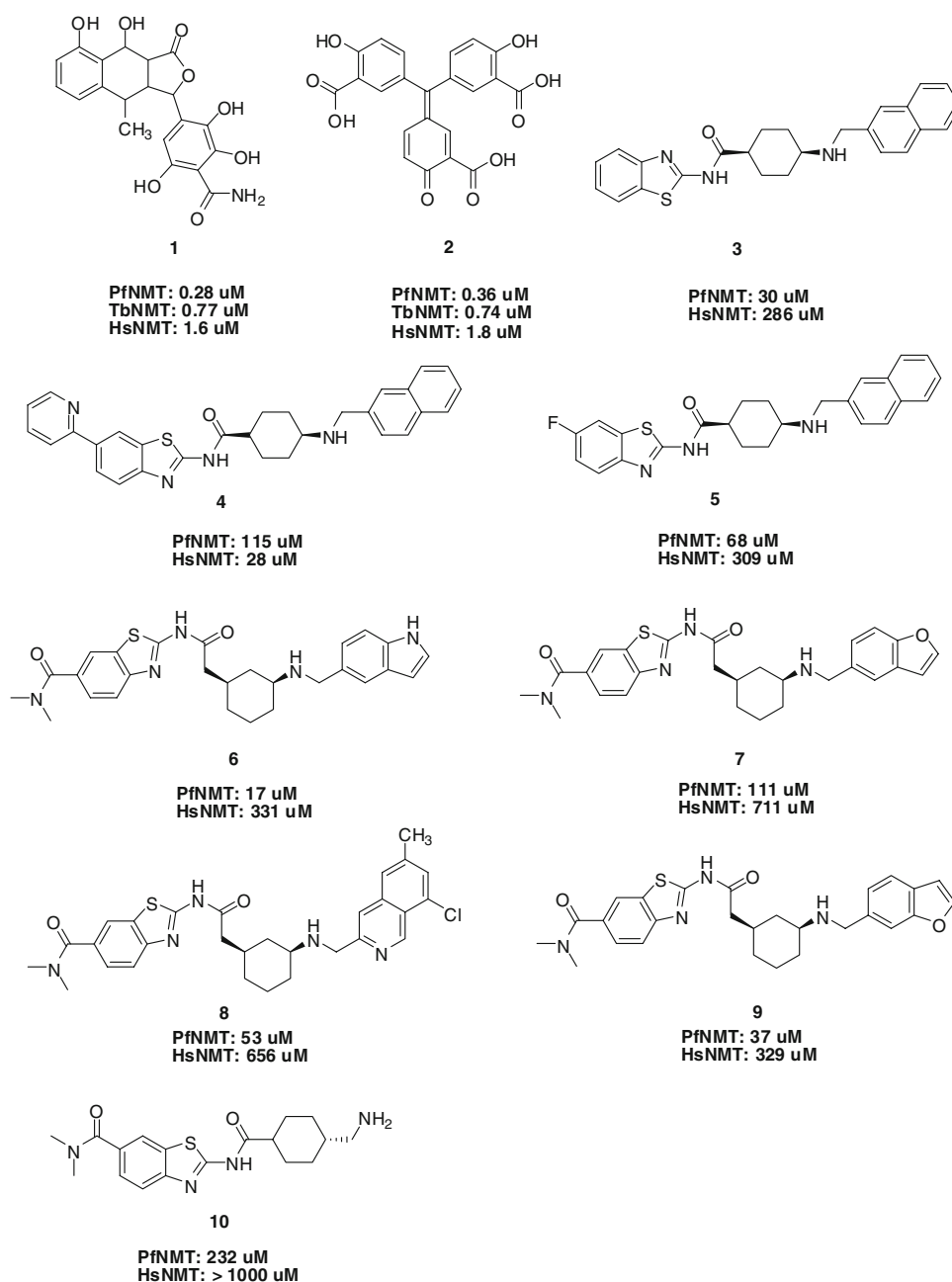
MCSS calculations

To explore the key regions in the active site that are necessary for ligand binding, the MCSS program [37] was employed to calculate the energetically favorable position and orientation of given functional groups in the active site of PfNMT, LmNMT and TbNMT. Four types of functional groups were chosen for the MCSS calculation: (1) hydrophobic functional groups: BENZ (benzene), CHEX (cyclohexane), PRPN (propane) and ILER (butane); (2) polar functional groups and solvent: PHEN (phenol), MEOH (methanol), THRR (ethanol) and WATR (water); (3) positively charged functional groups: MAMM (methyl ammonium) and Lysr (1-amino pentane); (4) negatively charged functional group: ACET (acetate ion). The binding site areas in the MCSS simulation were defined as an approximate 33 Å × 27 Å × 25 Å box for PfNMT, an approximate 29 Å × 22 Å × 20 Å box for LmNMT, and an approximate 35 Å × 31 Å × 29 Å box for TbNMT, which were centered around the grid points searched by InsightII/binding site analysis. Replicas of a given functional group were randomly distributed inside the binding site and then simultaneously and independently energy-minimized. Pairs of molecules were considered to be identical if the root-mean-square deviation (RMSD) between them was <0.2 Å, and in such cases, one of the pairs was eliminated. The above protocol was repeated 10 times for each of the functional groups to allow complete searching of the active site. All of the above calculations were performed using the CHARMM 22 force field and the MCSS 2.1 program.

Flexible docking analysis

The initial structures of compounds 1–10 (Fig. 1) were built by the builder module within InsightII software package. Then, the structures were subjected to energy minimization using the conjugate gradient method and CVFF force field in InsightII with a convergence criterion 0.001 kcal/mol Å. The flexible ligand docking procedure in the affinity module within InsightII was used to define the lowest energy position for the known inhibitors using a Monte Carlo docking protocol. All the residues in the active site of PfNMT and TbNMT were allowed to move. The solvation grid supplied with the affinity program was used. If the resulting inhibitor/enzyme system was within a predefined energy tolerance of the previous structure, the system was subjected to minimization. The resulting structure was accepted on the basis of energy check, which used the Metropolis criterion, and also a check of RMS distance of the new structure versus the structure found so far. The final conformation was obtained through a simulation annealing procedure from 500 to 300 K, and then

Fig. 1 Structures and biological activities (IC_{50} , μM) of ligands used in the docking study



5,000 rounds of energy minimization were performed to reach a convergence, where the resulting interaction energy values were used to define a rank order.

Results and discussion

Homology models of PfNMT, LmNMT and TbNMT

Since the accuracy of the homology model is related to the degree of sequence identity and similarity between template and target, the selection of a suitable template and an

optimal sequence alignment is essential to the success of homology modeling. To date, several X-ray crystal structures of CaNMT [22, 23] and ScNMT [20, 21, 24] have been determined, which are potential templates for protozoan parasitic NMTs modeling. The homology scores for the CaNMT compared with PfNMT, LmNMT and TbNMT were 43.0, 44.8, and 46.9%, respectively. For ScNMT, the scores are 46.8, 44.4, and 45.3%, respectively. Because CaNMT and ScNMT showed similar amino acid identity, both of them are chosen as templates for homology modeling. Moreover, modeling the ligand-bound conformation of proteins is more helpful in structure-based drug design.

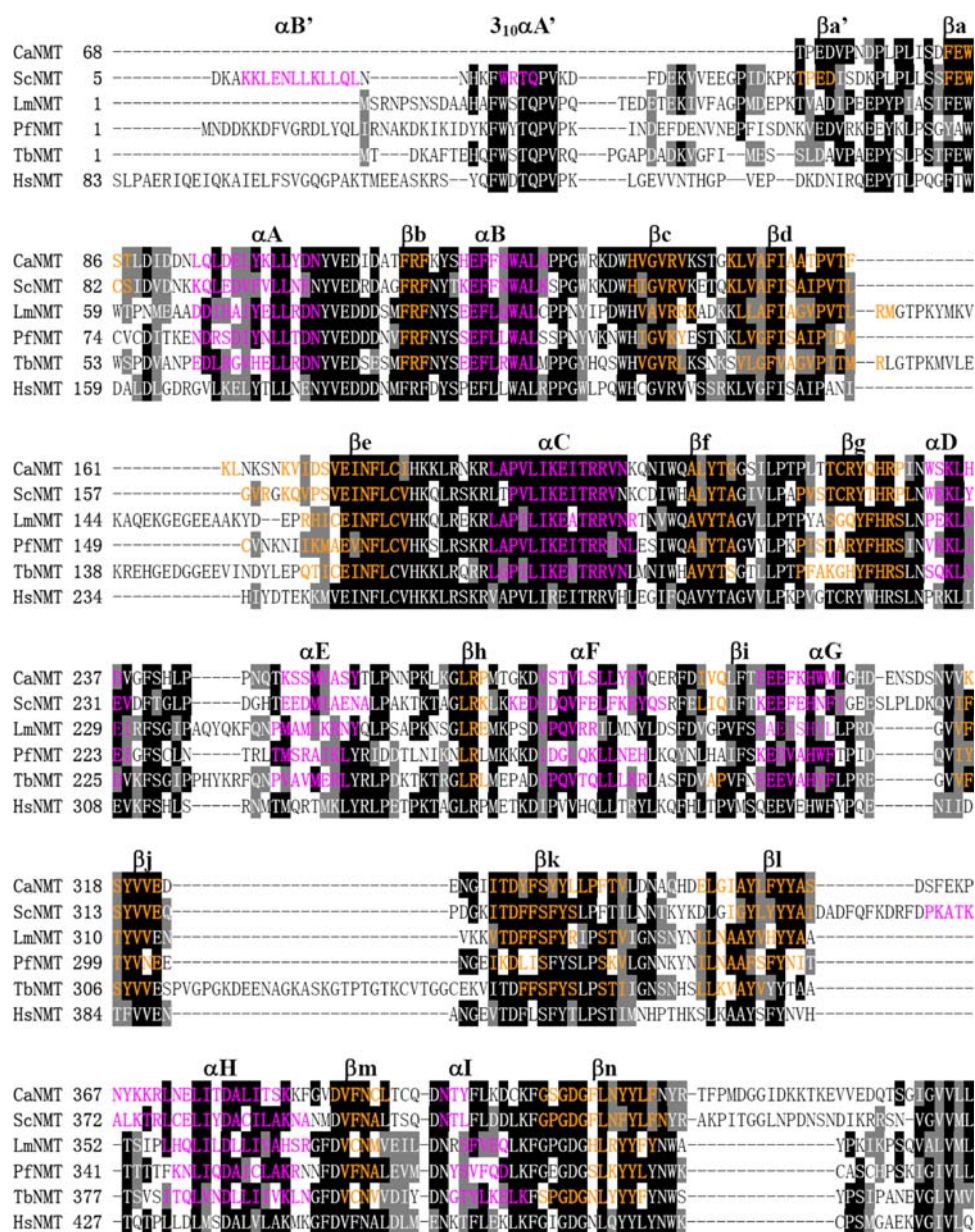
Therefore, instead of the apo-form, the crystal structures of CaNMT and ScNMT in complex with the small molecule inhibitors (PDB Code: 1IYL [22] and 2P6G [24], respectively) were eventually chosen as the template. The multiple sequence alignment of PfNMT, LmNMT, TbNMT, HsNMT, CaNMT and ScNMT is shown in Fig. 2, which is similar to alignments published by other groups [16].

MD simulation

To improve the relaxation of our modeled structures and to probe their intrinsic dynamics and structural stability to some extent, we performed the 1.0 ns MD simulation without any harmonic restraints on the model. Potential

energy and heavy atom RMSD from the energy-minimized model structure are calculated for each MD snapshot, which are two important criteria for the convergence of the free MD simulation. The potential energy of the three models decreased substantially in the first 200 ps of dynamics simulation and was stabilized after 600 ps equilibration. The relative structural drift or stability of the structures is measured as the RMSD of C α atoms from the initial structure as a function of time. As seen in Fig. 3, the structures of PfNMT and LmNMT deviate rapidly from the initial structure within the first 200 ps of the MD simulation. This increase in the RMSD value is due to optimization of interactions within the protein structure. After about 600 ps, the total RMSD of PfNMT and LmNMT model stabilized at around 2.8 Å and

Fig. 2 Sequence alignment of *N*-myristoyltransferase from *Plasmodium falciparum* (PfNMT), *Leishmania major* (LmNMT) and *Trypanosoma brucei* (TbNMT) with template proteins CaNMT (PDB code: 1IYL, from residues 68–451) and ScNMT (PDB code: 2P6G, from residues 5–455). Identical and similar residues are shown on a black and a light gray background, respectively. The nomenclature of the secondary structure is according to that of Bhatnagar et al. [20]. The α -helices are represented by magenta color and β -sheets are represented by orange color. The secondary structures are indicated along the top of alignment (α represents α -helix; β refers to β -sheet)



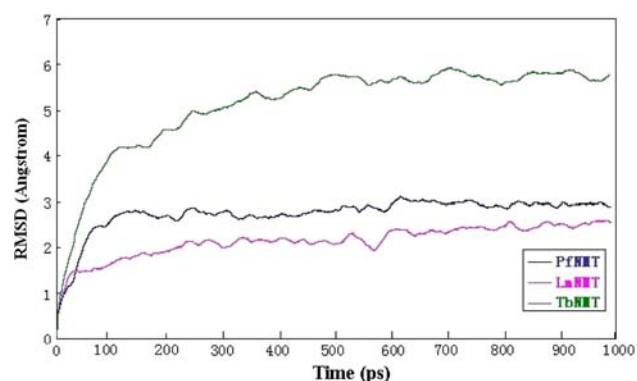


Fig. 3 The RMSD of the backbone alpha carbon atoms of the protein with respect to the initial equilibrated configuration as a function of time

2.6 Å, suggesting that a 1.0 ns unrestrained simulation was sufficient for stabilizing a fully relaxed model and the core structure of the protein was stable during the MD simulation. For the TbNMT model, the RMSD profile during MD simulation is different from the other two models. A plateau of ~ 5.7 Å RMSD value was achieved after 800 ps of MD simulation, which is much larger than the other two models. After analyzing the MD trajectory in detail, the large RMSD value of TbNMT is largely attributed to the long loop region between β_j and β_k . Because this loop is a large insertion, there was no corresponding structural information in the template proteins. During the MD simulation, the extended conformation of the loop was switched to a coiled conformation, leading to the decrease of the potential energy.

Model validation

The stereochemical quality of the modeled structures was checked by the ProStat module. No bond lengths and no bond angles were significantly different from average values calculated from known protein structures. The Ramachandran plots for local backbone conformation of each residue in the final models were produced by

PROCHECK (Table 1; Fig. 4). In PfNMT model, ϕ and ψ dihedral angles of 98.7% of the total residues were located within the allowed regions (83.3% most favored) of the Ramachandran plot. While in TbNMT model, 82% (366 residues) were in the most favoured regions with only 1.0% (4 residues) in disfavoured regions. In LmNMT model, 79% (230 residues) were in the most favoured regions with only 1.6% (7 residues) in disfavoured regions. The compatibility between the amino acid sequence and the environment of the amino acid side chains in the model is another validation criterion. The Profiles-3D scores (1D–3D compatibility score, S) of PfNMT, LmNMT and TbNMT were 175, 175 and 180, respectively, compared with the expected high scores of 187, 192 and 203 and the expected low scores of 84, 86 and 92, respectively. The 3D Profile scores for the compatibility of three sequences with their corresponding molecular models (Fig. 5) were within the limits of an acceptable value ($S > 0$).

Model description

The final structures of PfNMT, LmNMT and TbNMT are presented in Fig. 6. The secondary structures of modeled proteins are defined by the Kabsch and Sander method [38]. Besides the N-terminal region (absent in most of the reported crystal structures), CaNMT and ScNMT comprise of 9 α -helices and 14 β -sheets. Likewise, the three modeled enzymes appear to fold into 9 α -helices and 15 β -sheets. The additional β -strand of the models is located between β_k and β_l . The models of PfNMT, LmNMT and TbNMT consist of a large saddle-shaped β -sheet which dominates the core of the structure and is surrounded several helices. All the models reveal internally pseudo-twofold symmetry: the topological motifs in the N-terminal half are repeated in the C-terminal half. These results indicate that the overall structure of the predicted proteins show common 3D folding pattern compared with the crystal structures of fungal NMTs. However, variation arises in several ways. For all the three models, there is a 17-residue gap (between

Table 1 Model validation data of the PfNMT, LmNMT and TbNMT models as compared with the template proteins

	PfNMT	LmNMT	TbNMT	CaNMT	ScNMT
Ramachandran plot					
Most favored regions (%)	83.3	79.0	82.0	75.7	85.3
Additional allowed regions (%)	13.6	14.3	13.3	21.6	13.6
Generously allowed regions (%)	1.8	5.1	3.7	2.4	0.8
Disallowed regions (%)	1.3	1.6	1.0	0	0.3
Profile_3D					
Calculated scores	175	175	180	175	192
Expected high scores	187	192	203	177	199
Expected low scores	84	86	92	79	70

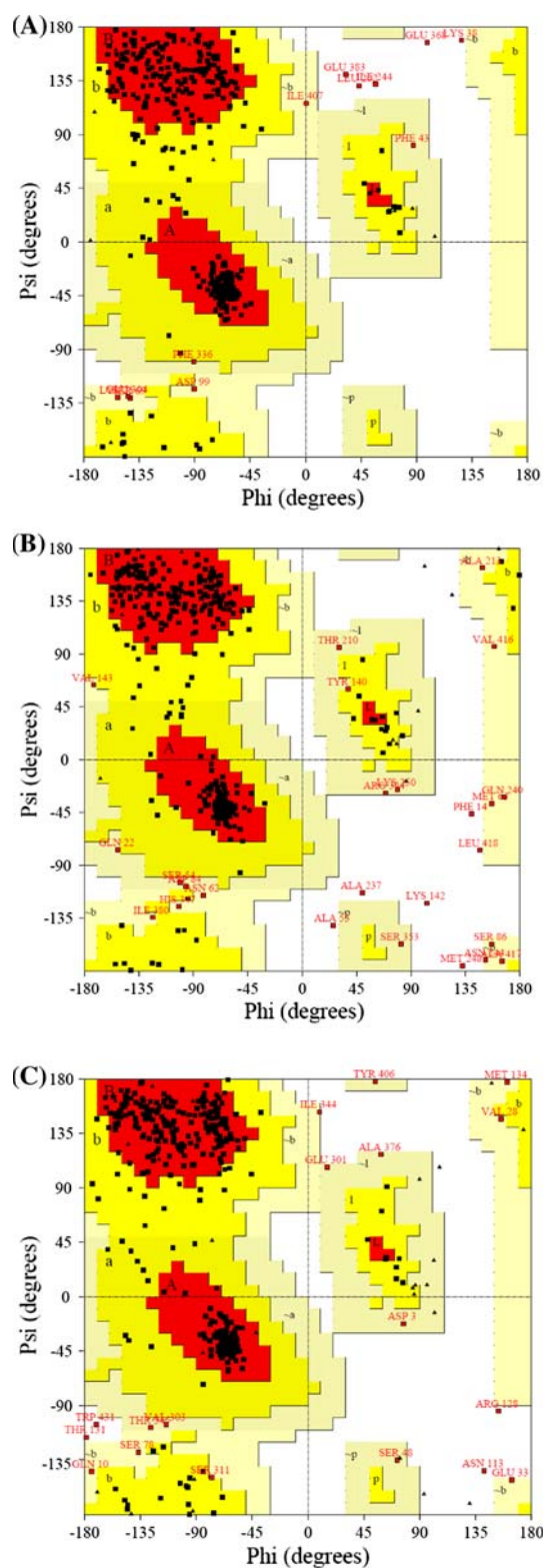


Fig. 4 Ramachandran plots obtained for the models of PfNMT, LmNMT and TbNMT. The most favorable regions are in red, favourable regions in yellow, allowed regions in tan

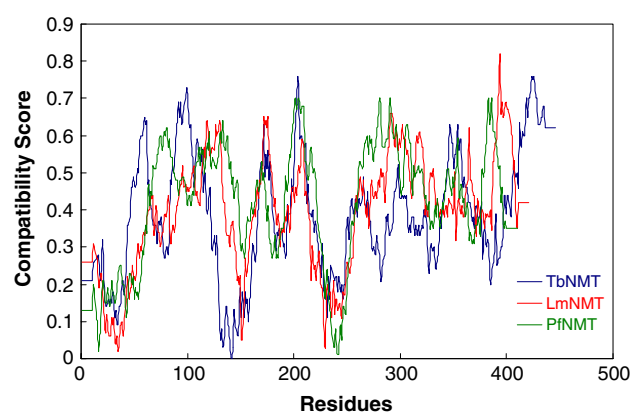


Fig. 5 The profile_3D plots of our modeled structures for PfNMT, LmNMT and TbNMT. Residues with positive compatibility score are reasonably folded

β l and α H) and a 14-residue gap (between β n and C-terminus) with fungal NMTs. These two gaps are near to the non-peptide inhibitor binding site, which may affect the conformation of the active site, and thus influence the ligand specificity and selectivity of parasitic NMTs. For the LmNMT and TbNMT model, there is a large insertion between β d and β e, which is far away from the active site and might have little influence on ligand binding. The major difference between the TbNMT model and the other two lies in the large insertion (28 residues) between β j and β k. This insertion is unique to TbNMT enzyme and greatly affected the MD properties. However, this loop region is exposed on the molecular surface and also far away from ligand binding site.

Active sites of PfNMT, LmNMT and TbNMT

All of the possible ligand binding cavities on the PfNMT, LmNMT and TbNMT models were searched by the binding site analysis program within InsightII. Four possible cavities in the PfNMT model were found. The largest cavity (Fig. 7a) with 940 grid points was the substrate-binding pocket, which is located in the long, deep groove on the surface of PfNMT. The other three cavities were filled with 121, 96, and 64 grid points, respectively. These small cavities were far away from the substrate-binding site. For the LmNMT model, five cavities were detected with 801, 430, 92, 88 and 82 grid points, respectively. The largest cavity (Fig. 7b) is the substrate-binding pocket. On the molecular model of TbNMT, five possible cavities were identified. The largest cavity filled with 1,066 grid points was also the substrate-binding pocket, as shown in Fig. 7c.

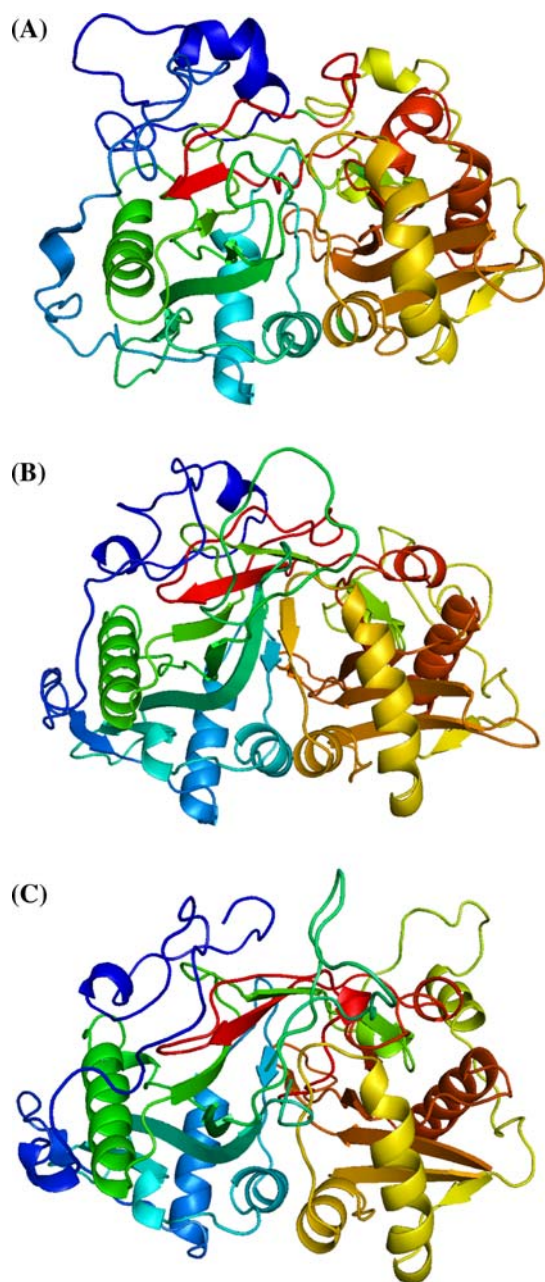


Fig. 6 Ribbon schematic representations of the refined homology model of PfNMT (a), LmNMT (b) and TbNMT (c). Images are generated using Pymol (www.pymol.org)

The other four cavities with 417, 309, 265, and 175 grid points were also far away from the substrate-binding site. So the largest cavity involved in substrate binding and catalytic reactions was chosen as the active site for the future inhibitor design. The active sites of three models show similar topology with those of CaNMT and PfNMT. The substrate-binding pocket is located between two topologically identical subunits, which is a long, curved groove with a deep, narrow-necked pocket at its center.

According to the crystal structures of CaNMT and PfNMT, the N-terminal half forms most parts of the myristoyl-CoA binding site, while the C-terminal half contributes largely to the peptide binding site. The non-peptide inhibitors are situated in the central pocket of the substrate binding site.

MCSS functional maps for the active site of PfNMT, LmNMT and TbNMT

The MCSS method was used to determine the favorable binding positions and orientations for the diverse functional groups with respect to the active site of PfNMT, LmNMT and TbNMT. The total numbers and ranges of energies of the minima found for the various molecular probes are summarized in Table 2. The MCSS functional groups were mapped into the active site of three models. The resulting molecular probe maps were examined using clustering, diversity analysis, and computer graphics. Firstly, the clusters were analyzed visually in the context of the protein structure. Secondly, the clusters were also analyzed quantitatively with one half the solvation enthalpy ($\Delta H/2$) of the group as a cutoff energy [39]. Thirdly, the distribution of the clusters and groups with lowest interaction energy was analyzed in detail to determine the important binding sites.

The active site of PfNMT

The crystal structures of ScNMT and CaNMT reveal two important sites for catalytic activity. Firstly, the backbone amides of F170 and L171 in ScNMT form an oxyanion hole which polarizes the reactive thioester carbonyl of myristoyl-CoA [21]. Secondly, the C-terminal carboxylate of NMT was reported to play an important role in the catalytic mechanism and ligand binding [20]. For example, the HB interaction between benzofuran inhibitors and the C-terminal carboxylate of Leu451 in CaNMT is essential for the enzyme inhibitory activity [28]. The minima with the most favorable interaction energies for the ring functional groups (i.e., benzene, cyclohexane, and polar phenol) were located in the S1 pocket (Fig. 7a) lined with hydrophobic residues such as Phe103, Phe105, Phe111, Phe162, Phe212, Phe226, Leu317, Leu330, Phe334, Phe336 and Leu388. The lowest-energy minima of alkyl functional groups (i.e., propane and butane) were also distributed into this region. The region displaying the second most favorable interaction for these hydrophobic and bulky functional groups was located in the S3 pocket (Fig. 7a), which is defined by Ile82, Leu163, Val165, Ile179 and Ala198. The polar functional groups containing hydrogen-bond donors and acceptors (i.e., water, methanol, and ether) were used to explore the hydrogen-bonding (HB) sites. The lowest energy minima of all three polar functional groups were mainly distributed in the S2 and the S4 pockets. In the S2

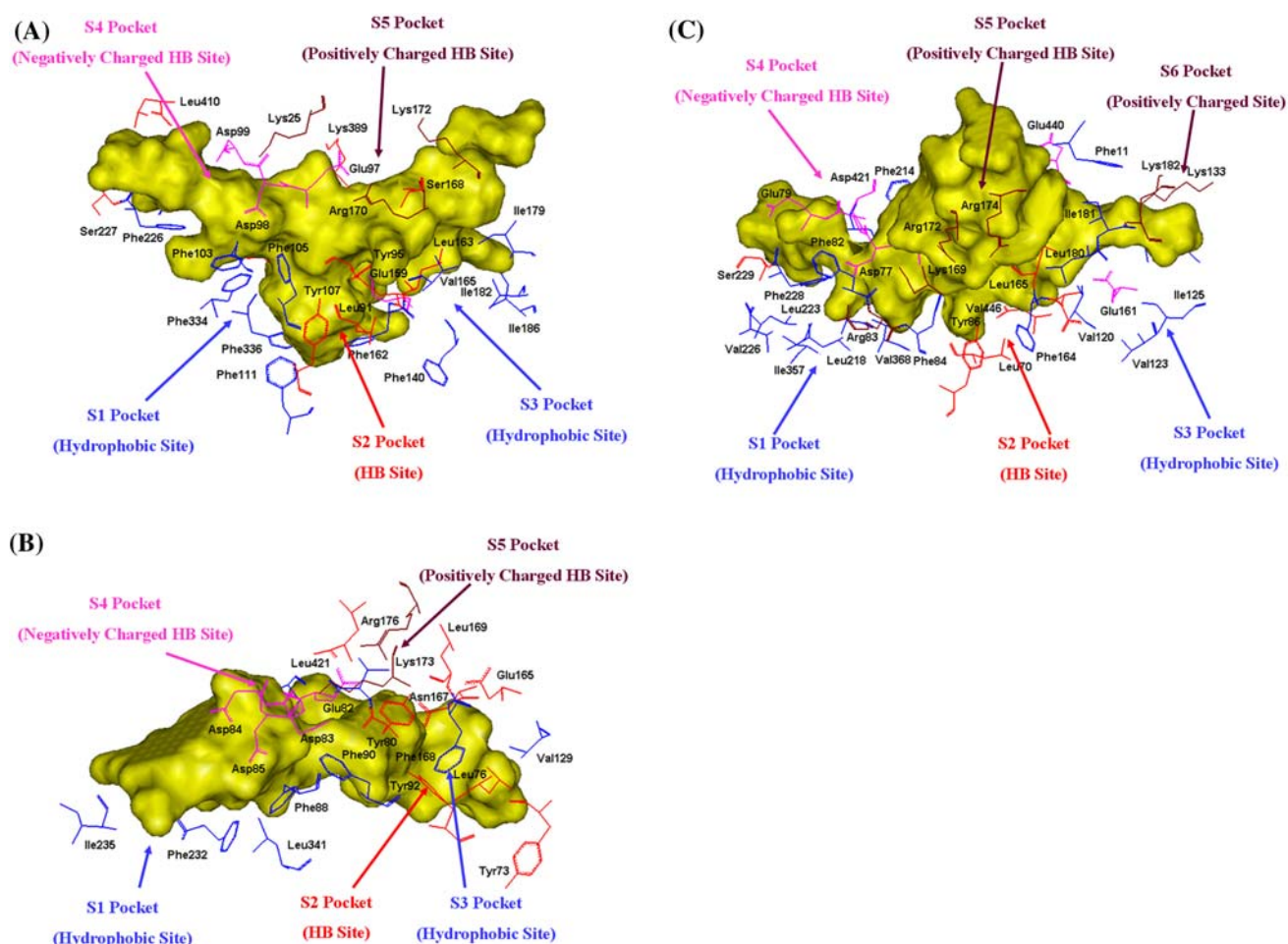


Fig. 7 Surface showing of the active site of PfNMT (**a**), LmNMT (**b**) and TbNMT (**c**). The surface is oriented to the position in which important residues are showed clearly. Important residues having favorable interaction energies with MCSS functional groups are displayed in *line* mode. Residues involved in hydrophobic site are

colored *blue*; Residues involved in hydrogen-bonding site are colored *red*; Residues involved in negatively charged site are colored *magenta*; Residues involved in positively charged site are colored *dark brown*; Residues with dual function are colored according to the interaction energies with MCSS functional groups

pocket, polar minima with lowest energy formed HB interactions with Leu91 (backbone carbonyl), Tyr107, Asn161, Leu163 (backbone carbonyl), Glu159 and Thr197. It is worth noting that the backbone amide of conserved residue Leu163 (corresponding to Leu171 in ScNMT) contributes to forming an oxyanion hole, which is important in the catalytic reaction of NMT [21]. Another HB site in the S4 pocket was defined by Thr211, Ser217 and the C-terminal residue Leu410 (carboxyl group), which might function as HB donors or acceptors in rational inhibitor design. Because the C-terminal carboxylate of NMT is important in the catalytic mechanism and ligand binding [20], the carboxylate of Leu410 in PfNMT should be considered as an important HB site in rational inhibitor design. The minima with the most favorable interaction energies for the positively charged functional groups (i.e., methyl ammonium, and 1-amino pentane) were also

located in the S4 pocket, which were surrounded by three sequential negatively charged residues (Glu97, Asp98 and Asp99). Thus, the S4 pocket might serve as a negatively charged HB site. The minimum of positively charged functional groups displaying the second most favorable interaction energies formed electrostatic interactions with Glu159 in the S2 pocket, which indicated that Glu159 had dual function and could form electrostatic and HB interaction with inhibitors. For the negatively charged functional groups, the minima with the lowest interaction energies were located in the S5 pocket, which is defined by Lys25, Arg170, Lys389 and Lys172. Moreover, several minima of polar functional groups were found located in this region and formed HB interactions with Lys25, Lys389 and Ser118, which indicated that the S6 pocket was a positively charged HB site and had dual function in inhibitor design.

Table 2 Summary of results for the functional groups used in the MCSS calculations

MCSS functional groups ^a	$\Delta H/2^b$ (kcal/mol)	Initial number of copies	Minima with interaction energy <0	Energy range (kcal/mol)	Minima with interaction < $\Delta H/2$
PfNMT					
BENZ	−3.8	1,000	285	−3.5 to −15.7	279
CHEX	−4.0	1,000	295	−0.7 to −10.3	112
PRPN	−2.7	1,000	280	−3.6 to −7.9	280
ILER	−3.1	1,000	499	−6.5 to −9.1	499
PHEN	−6.8	1,000	409	−12.1 to −26.1	409
MEOH	−5.3	1,000	399	−9.3 to −26.6	399
THRR	−6.3	1,000	460	−10.3 to −24.9	460
WATR	−5.0	1,000	346	−9.1 to −28.7	346
ACET	−46.5	1,000	92	−0.0 to −62.8	22
MAMM	−37.5	1,000	139	−0.4 to −96.9	31
LYSR	–	1,000	409	−27.5 to −84.6	–
LmNMT					
BENZ	−3.8	1,000	226	−4.3 to −10.4	126
CHEX	−4.0	1,000	109	−0.1 to −9.5	35
PRPN	−2.7	1,000	127	−2.8 to −7.0	127
ILER	−3.1	1,000	226	−4.3 to −8.0	226
PHEN	−6.8	1,000	195	−0.6 to −11.5	156
MEOH	−5.3	1,000	172	−0.3 to −15.6	166
THRR	−6.3	1,000	440	−4.7 to −16.0	386
WATR	−5.0	1,000	184	−0.3 to −23.7	123
ACET	−46.5	1,000	157	−2.2 to −68.1	49
MAMM	−37.5	1,000	95	−0.8 to −86.2	38
LYSR	–	1,000	346	−6.7 to −9.9	–
TbNMT					
BENZ	−3.8	1,000	277	−0.7 to −19.3	169
CHEX	−4.0	1,000	378	−3.0 to 9.8	167
PRPN	−2.7	1,000	383	−4.2 to −8.1	383
ILER	−3.1	1,000	414	−4.9 to −9.2	414
PHEN	−6.8	1,000	446	−14.7 to −40.2	446
MEOH	−5.3	1,000	399	−13.0 to −39.5	399
THRR	−6.3	1,000	329	−15.9 to −40.0	329
WATR	−5.0	1,000	366	−11.7 to −43.6	366
ACET	−46.5	1,000	154	−0.1 to −113.5	38
MAMM	−37.5	1,000	161	−0.6 to −133.9	77
LYSR	–	1,000	430	−70.6 to −128.3	–

Results are given for the PfNMT, LmNMT and TbNMT structures

^a See “[Materials and methods](#)” for the functional group definition

^b Values of $\Delta H/2$ for the MCSS functional groups were obtained from ref. [39]

The active site of LmNMT

The active site of LmNMT is narrower than that of PfNMT (Fig. 7b). However, the low-energy minima for the MCSS functional groups showed similar distribution with those of PfNMT. The minima with lowest interaction energies for hydrophobic and bulky functional groups were mainly

distributed in the S1 and S3 pockets (Fig. 7b). The S1 pocket was defined by Phe88, Phe90, Phe232, Ile235, Leu341 and Ile380. The S3 pocket was much smaller compared to the S1 pocket and lined with Val81, Leu76, Phe116, Val129, and Leu169. The minima with lowest interaction energies for polar functional group were located in the S2 pocket and form HB interactions with Tyr73,

Leu76 (backbone carbonyl), Tyr80, Tyr92, Glu165 and Asn167. Similarly, the S4 pocket was also a negatively charged HB site. Three conserved aspartate (Asp83, Asp84 and Asp85) interacted with the positively charged minima with lowest interaction energies. Moreover, several polar minima were found to form HB interaction with Glu82 and Leu421 (C-terminal carboxylate) in the S4 pocket. The low energy minima of the negatively charged functional group were mainly distributed in the S5 pocket and form electrostatic interaction with Lys173 and Arg176. Lys173 and Leu169 (backbone carbonyl as part of oxyanion hole) in the S5 pocket were also found to form HB interaction with some polar minima with low energies.

The active site of TbNMT

For the active site of TbNMT, similar functional regions were obtained from MCSS calculations (Fig. 7c). The S1 and S3 pockets were identified as the hydrophobic sites. The S1 pocket was lined with hydrophobic residues such as Phe82, Phe214, Leu218, Phe228, Leu223, Val226, Ile357, Val368, and Phe417. The S3 pocket was relatively small and was defined by Phe11, Val120, Val123, Ile125, Phe164, Leu180, and Ile181. Most of the residues involved in the HB interaction with polar minima were located in the S2 pocket. Leu70, Tyr86, Leu165 (backbone carbonyl as part of oxyanion hole), Glu161 and Val446 (C-terminal carboxylate) were important HB sites for the inhibitor design. In the S4 pocket, Asp77 and Glu79 were identified as negatively charged sites, while Tyr213 and Ser229 were served as HB residues. Unlike the active site of PfNMT and LmNMT, two positively charged sites were identified. One positively charged site was located in the S5 pocket, and low energy minima of acetate ion formed electrostatic interactions with Lys169, Arg172 and Arg174. The other positively charged site was characterized by Lys133 and Lys182, which was located in the additional S6 pocket.

Binding mode, structure–activity relationship and selectivity of known inhibitors

Recently, selective inhibitors of PfNMT and TbNMT have been identified by a ‘piggy-back’ approach [33, 34]. High-throughput screening was performed on a range of anti-fungal compounds, which are previously described as fungal NMT inhibitors. Up to now, rational design of parasitic NMT inhibitors has not been reported. Therefore, the investigation of the binding mode of known inhibitors is useful to identify key residues involved in ligand binding and provide straightforward information for structure-based drug design. Before we perform the docking studies, the selection of an appropriate docking method is of great importance. In our previous studies [40], the InsightII/

affinity method has been proved to be one of the best docking approaches, which can reproduce the position of benzofuran inhibitor in the crystal structure of 1IYL with the RMSD value of 1.259 Å. Moreover, the inhibitor recognition and binding is a process of “induced-fit”, the conformation of both target enzyme and inhibitor would be changed during the enzyme-inhibitor interaction. The flexibility of both active site of the target enzyme and the inhibitor is taken into account in the affinity method, which is especially powerful for a homology model.

Compounds **1–10** were docked into the active site of PfNMT (Fig. 8) and the calculated interaction energies of each compound are given in Table 3. Among the 10 compounds, only the inhibitory activities against TbNMT have been determined for compounds **1** and **2**. They were also docked into the active site of TbNMT.

Figure 8a shows the docking binding mode of compound **1**, the most potent PfNMT inhibitor, in the active site of PfNMT. The inhibitor was stabilized by HB and hydrophobic interactions. Five hydrogen bonds were formed between inhibitors and the residues in the active site. The C4 and C5 hydroxyl group of the tricyclic ring formed two hydrogen bonds with Leu91 (backbone carbonyl) and Tyr107 in the S2 pocket, respectively. The C2-hydroxyl hydrogen of trihydroxybenzamide made a hydrogen bond with phenolic oxygen of Tyr95 (pocket S2), and the amide group formed two hydrogen bonds with Lys389 (pocket S5). Several hydrophobic interactions were formed between the tricyclic ring and Leu91, Phe105 (pocket S1) and Leu163 (pocket S3). The phenyl group of trihydroxybenzamide formed van der Waals interactions with Ala198, Val200, and Leu202 (pocket S3). The binding mode of **1** within the TbNMT cavity is similar to that observed for binding to PfNMT. Leu91, Tyr95 and Tyr107 of PfNMT are conserved residues (corresponding to Leu70, Tyr74 and Tyr86 in TbNMT), and they also formed HB interactions with **1**. Although Lys389 of PfNMT is replaced by Tyr425 in TbNMT, the HB interactions with compound **1** is retained. The phenol hydrogen and backbone NH of Tyr425 in TbNMT formed two hydrogen bonds with **1**. The comparison of the binding mode of **1** with PfNMT and TbNMT shows that the main difference is due to the van der Waals interaction with the phenyl group of trihydroxybenzamide. The presence of Ala198 and Val200 in PfNMT, instead of Ser200 and Thr202 in TbNMT, allows a better contact, which might explain a slightly decrease of binding affinity of **1** for TbNMT. Compound **1** showed about sixfold selectivity for PfNMT over HsNMT. Most of the residues involved in ligand binding are conserved between PfNMT and HsNMT, except that Lys389 in PfNMT was replaced by Gln475 in HsNMT. The difference of the length of side chain between Lys389 and Gln475 might result in the loss of hydrogen

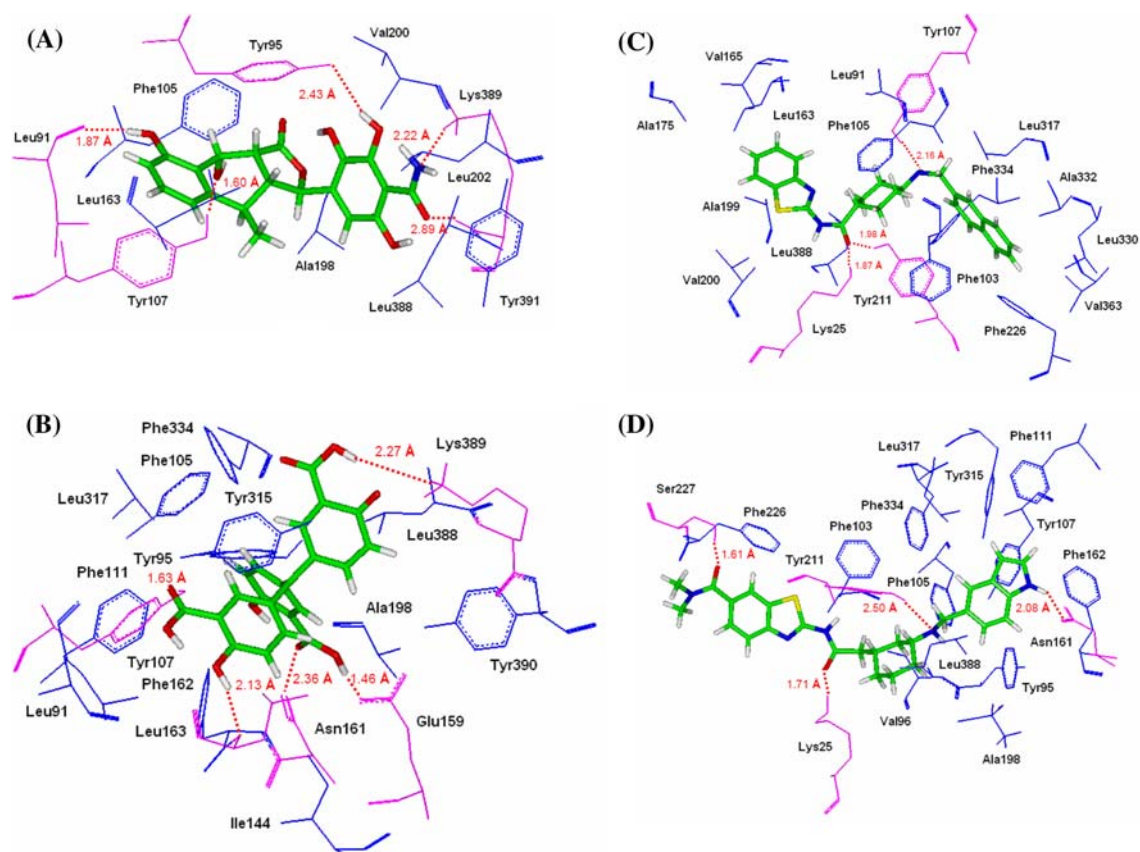


Fig. 8 The docking conformations of compound **1** (a), compound **2** (b), compound **3** (c) and compound **6** (d) in the active site of PfNMT. The residues within 4 Å of the inhibitor are displayed and the

inhibitors are shown in *stick* mode. Hydrogen bonds are displayed in *red dotted lines* with bond length values

Table 3 Calculated interaction energies (kcal/mol) for the complexes of compounds **1–10** with the active site of PfNMT

Compounds	E_{vdw}	E_{elect}	E_{total}
1	−57.8	−79.7	−137.5
2	−92.1	−32.7	−124.8
3	−69.9	−31.9	−101.8
4	−60.5	−18.4	−78.9
5	−65.7	−23.5	−89.2
6	−83.1	−36.0	−119.1
7	−63.1	−18.5	−81.6
8	−76.5	−17.8	−94.3
9	−78.1	−35.5	−113.6
10	−55.9	−10.5	−66.4

bond between the amide oxygen atom of **1** and the amino group of Gln475 of HsNMT.

Compound **2** occupied almost the same binding pocket as **1**, but the binding mode differed significantly (Fig. 8b). Five hydrogen bonds were observed between **2** and PfNMT. The hydroxyl and carboxy group of bis-2-hydroxybenzoic acid formed four hydrogen bonds with Tyr107, Glu159,

Asn161 and Leu163 in the S2 pocket. The carbonyl oxygen atom made a hydrogen bond with the amino group of Lys389 (pocket S5). The three phenyl groups of **2** were stabilized by the hydrophobic interaction with surrounding residues lined with Ala198 (pocket S3), Phe105, Leu388, Phe334, and Phe162 (pocket S1). The interactions between compound **2** and TbNMT is very similar. The slightly decrease of the binding affinity might be attributed to the decreased hydrophobic interaction, because Ala198 and Phe334 in PfNMT were replaced by Ser200 and Tyr370 in TbNMT respectively. For HsNMT, the loss of hydrogen bond between Compound **2** and Gln475 (corresponding to Lys389 in PfNMT) might result in fivefold decrease of binding affinity.

Compounds **3–5** are identical except for the C-6 substitution on the benzothiazole ring. The docking results revealed that compound **3** made three hydrogen bonds with PfNMT. The amide oxygen atom formed two hydrogen bonds with Lys25 (pocket S5) and Tyr211 (pocket S4). The secondary amine formed another hydrogen bond with Tyr107 (pocket S2). It is worth noting that Lys25 is a specific residue for PfNMT (corresponding to Ser116 in HsNMT) and the loss of the hydrogen bond might explain

the tenfold selectivity for PfNMT over HsNMT. The benzothiazole ring is stabilized by conserved hydrophobic residues in the S3 pocket such as Leu91, Leu163, Val165, Ala175, Ala198 and Val200. The cyclohexyl group of **3** made hydrophobic contacts with Phe103, Phe105 and Leu388. The naphthyl group was located into the S1 pocket lined with Phe226, Leu317, Leu330, Ala332 and Phe334. The modifications at the C-6 position of the benzothiazole group by fluorine (compound **4**) and 2-pyridinyl (compound **5**) led to the two- to four-fold decrease of inhibitory activity. From the docking results, the benzothiazole group is surrounded by Leu91, Leu163 and Val165, and there is no space for a bulky group. The C-6 position is near to the backbone carbonyl group of Leu163, an electrostatic negative group is unfavorable at this position. Therefore, a fluorine atom with negative charge and a bulky 2-pyridinyl group at the C-6 position of benzothiazole ring could make the amide and secondary amino group move away from Lys25, Tyr107 and Try211, and some HB interactions might be lost. Moreover, the modification of C-6 position resulted in the reversal of selectivity between PfNMT and HsNMT1. It is supposed that new HB interactions might be formed between **4** or **5** and HsNMT after moving away from the binding region of **3**.

Compounds **6–10** all contain a cyclohexyl linker with 1*R*, 3*S* stereochemistry (as compared with 1*S*, 4*S* in compounds **3–5**) and a dimethylamide as the C-6 benzothiazole substituent. These compounds were also stabilized by hydrophobic and HB interactions with PfNMT. However, compounds **6–10** showed a different binding mode as compared with compounds **3–5**. They were found in the long groove of PfNMT with extended conformation, which were similar to the binding mode of peptide inhibitors with CaNMT and ScNMT. Four hydrogen bonds were observed between **6** and PfNMT. The dimethylamide group was known to form favorable binding interactions in the peptide-binding pocket of CaNMT [34]. In the present investigation, the amide oxygen atom of the dimethylamide group made a hydrogen bond with Ser227 (pocket S4), and the two methyl groups established van der Waals interactions with Leu229. Another amide oxygen atom and the secondary amino group formed two hydrogen bonds with Lys25 (pocket S5) and Tyr211 (pocket S4), respectively. Similarly, the HB interaction with the specific residue Lys25 could account for the 20-fold selectivity of **6** between PfNMT and HsNMT. The cyclohexyl group of **6** was stabilized by hydrophobic interaction with Phe103 and Leu388, and the indole ring was located in a hydrophobic pocket lined with conserved aromatic residues in the S1 pocket such as Phe105, Phe111, Phe162 and Phe334. The NH of indole ring functioned as a hydrogen bond donor and made a hydrogen bond with the carboxyl group of Asn161. When the NH group was replaced by an oxygen

atom (compound **7**), the HB interaction was lost, which led to the 6.5-fold decrease of inhibitory activity. When the oxygen atom in benzofuran ring of compound **7** was moved to the other side (compound **9**), a novel HB interaction was observed between the oxygen atom and Tyr107, and as a result, the inhibitory activity of compound **9** was improved. For compound **8**, a better lipophilic stabilization of the 8-chloro-6-methylisoquinoline group with the hydrophobic pocket of PfNMT might explain a twofold increase of the inhibitory activity. Compound **10** is the least potent compound in the dataset with an aminomethyl group attached to the cyclohexyl group. The loss of hydrophobic and HB interaction observed in compounds **6–9** is probably the reason that accounts for the decreased binding affinity.

Implication for rational inhibitor design

Analysis of interactions between all the inhibitors and PfNMT indicates that hydrophobic and HB interactions are mainly responsible for inhibitor binding. Among these inhibitors, the total interaction energy correlates well with the IC₅₀ values. Although the total interaction energies obtained in the present docking study do not reproduce the real binding free energies, the relative values should be meaningful in rational inhibitor design. The selectivity of the PfNMT inhibitors over HsNMT is mainly attributed to the HB interaction with Lys25 and Lys389. The binding modes of the inhibitors are consistent with the results from MCSS calculations. The inhibitors form hydrophobic interaction with the S1 and S3 pocket. Residues in the S2, S4 and S5 pockets are responsible for the HB interaction with the inhibitors. There is a negatively charged (pocket S4) and a positively charged (pocket S5) pocket in the active site. However, no electrostatic interaction was observed between the current inhibitors and the S4 and S5 pockets. Thus, taking the electrostatic interaction into account would further improve the affinity of the inhibitors. Moreover, the C-terminal carboxylate plays an important role in catalytic mechanism and inhibitor design. The reported inhibitors could not form HB interactions with it. Therefore, in subsequent rational inhibitor design efforts, the C-terminal carboxylic group of the enzymes should be considered as an important HB site.

On the basis of the findings obtained in this study, we suggest the following strategies for the design of novel parasitic NMT inhibitors. Firstly, inhibitors should have enough hydrophobicity to interact with the S1 and S3 pockets. Second, HB interaction with C-terminal carboxylate (i.e., Leu410 in PfNMT) and oxyanion hole residues (i.e., Leu163 in PfNMT) seems to be necessary. Thirdly, additional HB interaction with the residues in the S2, S4, or S5 pocket would improve the affinity. In order to achieve selectivity over HsNMT, HB interaction with Lys25 or Lys389 is

helpful. Lastly, inhibitors could have more charged groups to interact with the residues in the S4 and/or S5 pockets.

Conclusion

NMT has been identified as a promising drug target in protozoan parasites and the structural information of parasitic NMTs is of great importance to design specific inhibitors. The 3D structures of PfNMT, LmNMT and TbNMT were constructed, for the first time, by homology modeling on the basis of the known crystal structures of fungal NMTs. The modeled structures were further refined by energy minimization and molecular dynamics simulation. MCSS functional maps reveal that PfNMT, LmNMT and TbNMT all share two hydrophobic pockets (pocket S1 and S3), a hydrogen-binding (HB) pocket (pocket S2), a negatively-charged HB pocket (pocket S4) and a positively-charged HB pocket (pocket S5). Flexible docking was used to study the binding mode of the reported PfNMT inhibitors. The calculated binding energies follow the same trend as the measured inhibitory activities. Although various inhibitors had distinct binding modes, they are all stabilized by the hydrophobic and HB interactions. The selectivity of inhibitors for either PfNMT or HsNMT was mainly attributed to HB interaction with Lys389 and Lys25. Up to now, rational design of parasitic NMTs inhibitors has not been reported, and the structural models in this study can be used in virtual screening or de novo inhibitor design for discovery of new lead compounds.

Acknowledgments This work was supported in part by the National Natural Science Foundation of China (Grant Nos. 30400567) and Shanghai Leading Academic Discipline Project (Project Nos. B906). We thank Dr. Zhanli Wang in NeoTrident Technology LTD. for his assistance in molecular dynamics simulations.

References

- Boutin JA (1997) Myristoylation. *Cell Signal* 9:15. doi:[10.1016/S0898-6568\(96\)00100-3](https://doi.org/10.1016/S0898-6568(96)00100-3)
- Farazi TA, Waksman G, Gordon JI (2001) The biology and enzymology of protein N-myristoylation. *J Biol Chem* 276:39501. doi:[10.1074/jbc.R100042200](https://doi.org/10.1074/jbc.R100042200)
- Bhatnagar RS, Schall OF, Jackson-Machelski E, Sikorski JA, Devadas B, Gokel GW, Gordon JI (1997) Titration calorimetric analysis of AcylCoA recognition by myristoyl-CoA:protein N-myristoyltransferase. *Biochemistry* 36:6700. doi:[10.1021/bi970311v](https://doi.org/10.1021/bi970311v)
- Rudnick DA, McWherter CA, Rocque WJ, Lennon PJ, Getman DP, Gordon JI (1991) Kinetic and structural evidence for a sequential ordered Bi Bi mechanism of catalysis by *Saccharomyces cerevisiae* myristoyl-CoA:protein N-myristoyltransferase. *J Biol Chem* 266:9732
- Knoll LJ, Johnson DR, Bryant ML, Gordon JI (1995) Functional significance of myristoyl moiety in N-myristoyl proteins. *Methods Enzymol* 250:405. doi:[10.1016/0076-6879\(95\)50088-X](https://doi.org/10.1016/0076-6879(95)50088-X)
- Olson EN, Towler DA, Glaser L (1985) Specificity of fatty acid acylation of cellular proteins. *J Biol Chem* 260:3784
- Towler DA, Adams SP, Eubanks SR, Towery DS, Jackson-Machelski E, Glaser L, Gordon JI (1987) Purification and characterization of yeast myristoyl CoA:protein N-myristoyltransferase. *Proc Natl Acad Sci USA* 84:2708. doi:[10.1073/pnas.84.9.2708](https://doi.org/10.1073/pnas.84.9.2708)
- Gordon JI, Duronio RJ, Rudnick DA, Adams SP, Gokel GW (1991) Protein N-myristoylation. *J Biol Chem* 266:8647
- Duronio RJ, Reed SI, Gordon JI (1992) Mutations of human myristoyl-CoA:protein N-myristoyltransferase cause temperature-sensitive myristic acid auxotrophy in *Saccharomyces cerevisiae*. *Proc Natl Acad Sci USA* 89:4129. doi:[10.1073/pnas.89.9.4129](https://doi.org/10.1073/pnas.89.9.4129)
- Giang DK, Cravatt BF (1998) A second mammalian N-myristoyltransferase. *J Biol Chem* 273:6595. doi:[10.1074/jbc.273.12.6595](https://doi.org/10.1074/jbc.273.12.6595)
- Rioux V, Beauchamp E, Pedrono F, Daval S, Molle D, Catheline D, Legrand P (2006) Identification and characterization of recombinant and native rat myristoyl-CoA: protein N-myristoyltransferases. *Mol Cell Biochem* 286:161. doi:[10.1007/s11010-005-9108-0](https://doi.org/10.1007/s11010-005-9108-0)
- Duronio RJ, Towler DA, Heuckeroth RO, Gordon JI (1989) Disruption of the yeast N-myristoyl transferase gene causes recessive lethality. *Science* 243:796. doi:[10.1126/science.2644694](https://doi.org/10.1126/science.2644694)
- Lodge JK, Jackson-Machelski E, Toffaletti DL, Perfect JR, Gordon JI (1994) Targeted gene replacement demonstrates that myristoyl-CoA: protein N-myristoyltransferase is essential for viability of *Cryptococcus neoformans*. *Proc Natl Acad Sci USA* 91:12008. doi:[10.1073/pnas.91.25.12008](https://doi.org/10.1073/pnas.91.25.12008)
- Weinberg RA, McWherter CA, Freeman SK, Wood DC, Gordon JI, Lee SC (1995) Genetic studies reveal that myristoyl-CoA:protein N-myristoyltransferase is an essential enzyme in *Candida albicans*. *Mol Microbiol* 16:241. doi:[10.1111/j.1365-2958.1995.tb02296.x](https://doi.org/10.1111/j.1365-2958.1995.tb02296.x)
- Gunaratne RS, Sajid M, Ling IT, Tripathi R, Pachebat JA, Holder AA (2000) Characterization of N-myristoyltransferase from *Plasmodium falciparum*. *Biochem J* 348:459. doi:[10.1042/0264-6021:3480459](https://doi.org/10.1042/0264-6021:3480459)
- Price HP, Menon MR, Panethymitaki C, Goulding D, McKean PG, Smith DF (2003) Myristoyl-CoA:protein N-myristoyltransferase, an essential enzyme and potential drug target in kinetoplastid parasites. *J Biol Chem* 278:7206. doi:[10.1074/jbc.M211391200](https://doi.org/10.1074/jbc.M211391200)
- Selvakumar P, Lakshmikuttyamma A, Shrivastav A, Das SB, Dimmock JR, Sharma RK (2007) Potential role of N-myristoyltransferase in cancer. *Prog Lipid Res* 46:1. doi:[10.1016/j.plipres.2006.05.002](https://doi.org/10.1016/j.plipres.2006.05.002)
- Hill BT, Skowronski J (2005) Human N-myristoyltransferases form stable complexes with lentiviral nef and other viral and cellular substrate proteins. *J Virol* 79:1133. doi:[10.1128/JVI.79.2.1133-1141.2005](https://doi.org/10.1128/JVI.79.2.1133-1141.2005)
- Georgopapadakou NH (2002) Antifungals targeted to protein modification: focus on protein N-myristoyltransferase. *Expert Opin Investig Drugs* 11:1117. doi:[10.1517/13543784.11.8.1117](https://doi.org/10.1517/13543784.11.8.1117)
- Bhatnagar RS, Futterer K, Farazi TA, Korolev S, Murray CL, Jackson-Machelski E, Gokel GW, Gordon JI, Waksman G (1998) Structure of N-myristoyltransferase with bound myristoylCoA and peptide substrate analogs. *Nat Struct Biol* 5:1091. doi:[10.1038/4202](https://doi.org/10.1038/4202)
- Farazi TA, Waksman G, Gordon JI (2001) Structures of *Saccharomyces cerevisiae* N-myristoyltransferase with bound myristoylCoA and peptide provide insights about substrate recognition and catalysis. *Biochemistry* 40:6335. doi:[10.1021/bi0101401](https://doi.org/10.1021/bi0101401)

22. Sogabe S, Masubuchi M, Sakata K, Fukami TA, Morikami K, Shiratori Y, Ebiike H, Kawasaki K, Aoki Y, Shimma N, D'Arcy A, Winkler FK, Banner DW, Ohtsuka T (2002) Crystal structures of *Candida albicans* *N*-myristoyltransferase with two distinct inhibitors. *Chem Biol* 9:1119. doi:[10.1016/S1074-5521\(02\)00240-5](https://doi.org/10.1016/S1074-5521(02)00240-5)
23. Weston SA, Camble R, Colls J, Rosenbrock G, Taylor I, Egerton M, Tucker AD, Tunnicliffe A, Mistry A, Mancina F, de la Fortelle E, Irwin J, Bricogne G, Pauptit RA (1998) Crystal structure of the anti-fungal target *N*-myristoyl transferase. *Nat Struct Biol* 5:213. doi:[10.1038/nsb0398-213](https://doi.org/10.1038/nsb0398-213)
24. Wu J, Tao Y, Zhang M, Howard MH, Gutteridge S, Ding J (2007) Crystal structures of *Saccharomyces cerevisiae* *N*-myristoyltransferase with bound myristoyl-CoA and inhibitors reveal the functional roles of the N-terminal region. *J Biol Chem* 282:22185. doi:[10.1074/jbc.M702696200](https://doi.org/10.1074/jbc.M702696200)
25. Ebiike H, Masubuchi M, Liu P, Kawasaki K, Morikami K, Sogabe S, Hayase M, Fujii T, Sakata K, Shindoh H, Shiratori Y, Aoki Y, Ohtsuka T, Shimma N (2002) Design and synthesis of novel benzofurans as a new class of antifungal agents targeting fungal *N*-myristoyltransferase. Part 2. *Bioorg Med Chem Lett* 12:607. doi:[10.1016/S0960-894X\(01\)00808-3](https://doi.org/10.1016/S0960-894X(01)00808-3)
26. Kawasaki K, Masubuchi M, Morikami K, Sogabe S, Aoyama T, Ebiike H, Niizuma S, Hayase M, Fujii T, Sakata K, Shindoh H, Shiratori Y, Aoki Y, Ohtsuka T, Shimma N (2003) Design and synthesis of novel benzofurans as a new class of antifungal agents targeting fungal *N*-myristoyltransferase. Part 3. *Bioorg Med Chem Lett* 13:87. doi:[10.1016/S0960-894X\(02\)00844-2](https://doi.org/10.1016/S0960-894X(02)00844-2)
27. Masubuchi M, Ebiike H, Kawasaki K, Sogabe S, Morikami K, Shiratori Y, Tsujii S, Fujii T, Sakata K, Hayase M, Shindoh H, Aoki Y, Ohtsuka T, Shimma N (2003) Synthesis and biological activities of benzofuran antifungal agents targeting fungal *N*-myristoyltransferase. *Bioorg Med Chem* 11:4463. doi:[10.1016/S0968-0896\(03\)00429-2](https://doi.org/10.1016/S0968-0896(03)00429-2)
28. Masubuchi M, Kawasaki K, Ebiike H, Ikeda Y, Tsujii S, Sogabe S, Fujii T, Sakata K, Shiratori Y, Aoki Y, Ohtsuka T, Shimma N (2001) Design and synthesis of novel benzofurans as a new class of antifungal agents targeting fungal *N*-myristoyltransferase. Part 1. *Bioorg Med Chem Lett* 11:1833. doi:[10.1016/S0960-894X\(01\)00319-5](https://doi.org/10.1016/S0960-894X(01)00319-5)
29. Ebara S, Naito H, Nakazawa K, Ishii F, Nakamura M (2005) FTR1335 is a novel synthetic inhibitor of *Candida albicans* *N*-myristoyltransferase with fungicidal activity. *Biol Pharm Bull* 28:591. doi:[10.1248/bpb.28.591](https://doi.org/10.1248/bpb.28.591)
30. Yamazaki K, Kaneko Y, Suwa K, Ebara S, Nakazawa K, Yasuno K (2005) Synthesis of potent and selective inhibitors of *Candida albicans* *N*-myristoyltransferase based on the benzothiazole structure. *Bioorg Med Chem* 13:2509. doi:[10.1016/j.bmc.2005.01.033](https://doi.org/10.1016/j.bmc.2005.01.033)
31. Renslo AR, McKerrow JH (2006) Drug discovery and development for neglected parasitic diseases. *Nat Chem Biol* 2:701. doi:[10.1038/nchembio837](https://doi.org/10.1038/nchembio837)
32. Bowyer PW, Tate EW, Leatherbarrow RJ, Holder AA, Smith DF, Brown KA (2008) *N*-Myristoyltransferase: a prospective drug target for protozoan parasites. *ChemMedChem* 3:402. doi:[10.1002/cmdc.200700301](https://doi.org/10.1002/cmdc.200700301)
33. Panethymitaki C, Bowyer PW, Price HP, Leatherbarrow RJ, Brown KA, Smith DF (2006) Characterization and selective inhibition of myristoyl-CoA:protein *N*-myristoyltransferase from *Trypanosoma brucei* and *Leishmania major*. *Biochem J* 396:277. doi:[10.1042/BJ20051886](https://doi.org/10.1042/BJ20051886)
34. Bowyer PW, Gunaratne RS, Grainger M, Withers-Martinez C, Wickramasinghe SR, Tate EW, Leatherbarrow RJ, Brown KA, Holder AA, Smith DF (2007) Molecules incorporating a benzothiazole core scaffold inhibit the *N*-myristoyltransferase of *Plasmodium falciparum*. *Biochem J* 408:173. doi:[10.1042/BJ20070692](https://doi.org/10.1042/BJ20070692)
35. Laskowski RA, MacArthur MW, Moss DS, Thornton JM (1993) PROCHECK: a program to check the stereochemical quality of protein structures. *J Appl Cryst* 26:283. doi:[10.1107/S0021889892009944](https://doi.org/10.1107/S0021889892009944)
36. Luthy R, Bowie JU, Eisenberg D (1992) Assessment of protein models with three-dimensional profiles. *Nature* 356:83. doi:[10.1038/356083a0](https://doi.org/10.1038/356083a0)
37. Miranker A, Karplus M (1991) Functionality maps of binding sites: a multiple copy simultaneous search method. *Proteins* 11:29. doi:[10.1002/prot.340110104](https://doi.org/10.1002/prot.340110104)
38. Kabsch W, Sander C (1983) Dictionary of protein secondary structure: pattern recognition of hydrogen-bonded and geometrical features. *Biopolymers* 22:2577. doi:[10.1002/bip.360221211](https://doi.org/10.1002/bip.360221211)
39. Evensen E, Joseph-McCarthy D, Weiss GA, Schreiber SL, Karplus M (2007) Ligand design by a combinatorial approach based on modeling and experiment: application to HLA-DR4. *J Comput Aided Mol Des* 21:395. doi:[10.1007/s10822-007-9119-x](https://doi.org/10.1007/s10822-007-9119-x)
40. Sheng C, Zhu J, Zhang W, Zhang M, Ji H, Song Y, Xu H, Yao J, Miao Z, Zhou Y, Lu J (2007) 3D-QSAR and molecular docking studies on benzothiazole derivatives as *Candida albicans* *N*-myristoyltransferase inhibitors. *Eur J Med Chem* 42:477. doi:[10.1016/j.ejmech.2006.11.001](https://doi.org/10.1016/j.ejmech.2006.11.001)